Journal of Power Sources 205 (2012) 32–47

Contents lists available at SciVerse ScienceDirect

Journal of Power Sources

journal homepage: www.elsevier.com/locate/jpowsour

Effects of serpentine flow-field designs with different channel and rib widths on the performance of a direct methanol fuel cell

Young-Chul Park[a,1], Purushothama Chippar[b], Sang-Kyung Kim[a], Seongyop Lim[a], Doo-Hwan Jung[a], Hyunchul Ju[b], Dong-Hyun Peck[a,*]

[a] Fuel Cell Research Center, Korea Institute of Energy Research (KIER), 152 Gajeong-ro, Yuseong-gu, 305-343 Daejeon, Republic of Korea
[b] Eco-Smart Power Lab, School of Mechanical Engineering, Inha University, 253 Yonghyun-dong, Nam-gu, 402-751 Incheon, Republic of Korea

ARTICLE INFO

Article history:
Received 22 October 2011
Received in revised form
27 December 2011
Accepted 28 December 2011
Available online 8 January 2012

Keywords:
Direct methanol fuel cell
Flow channel geometry
Channel and rib
Cell performance
Mass transport

ABSTRACT

This study experimentally and numerically investigates the effects of the four different types of serpentine flow-field geometry on the performance of a direct methanol fuel cells (DMFCs). To elucidate the effect of different channel/rib aspect ratios, the through/in-plane transport of methanol and air, the current density distribution, the anode and cathode polarization, the impedance and the cathode pressure drop are numerically and/or experimentally observed. The sub-rib convection significantly affects the cell performance with the serpentine flow fields. Thus, a narrow rib width and a suitable channel/rib aspect ratio are needed to increase the cell performance of serpentine DMFCs. This flow channel, for example, an F2-type flow channel (channel width: 1.0 mm, rib width: 0.5 mm), leads to formation of a narrower rib chain as well as a higher current density distribution in the rib, and thereby it brings about improvement of the two-phase flow in DMFCs, which is supported through the high performance difference in the high current density regions and the long-term stability test of 700 h.

1. Introduction

Direct methanol fuel cells (DMFCs) are attractive as a promising power source for portable multifunctional devices and light-duty vehicles because of easy storage of the fuel, light weight, small system size and high energy density [1]. The performance and durability of DMFCs depend on many factors, including the operating conditions, mass transport phenomena inside the cell, kinetics of the electrochemical reaction, membrane electrode assembly (MEA) and flow channel geometry [2].

The flow field channel, which is integrated into bipolar plates, is also an important component because it serves as a fuel or air distributor as well as a current collector. In general, the flow field channels influence the fuel and air distributions, the concentration polarization loss, the electrical current conduction, the heat conduction, etc. [3–9]. The flow field channel is especially important for water management inside the fuel cells since the products (CO_2 and H_2O) are removed through flow field channels. Therefore, an appropriate flow channel design is necessary for achieving high performance and durability of the cell as it resolves mass transport-related problems and improves the water management in the channel, the gas diffusion layer (GDL) and the catalyst layer (CL) [10].

Many researchers have studied the effects of flow channel geometry on the homogeneous distribution of the reactants and on cell performance. Shimpalee et al. [11] investigated the effects of the channel and rib cross-sectional areas on the reactant distribution and cell performance with serpentine flow field patterns and showed that narrower channels with wider rib spacing resulted in higher performance. Yoon et al. [12] reported that a narrower rib width led to improved performance of proton exchange membrane fuel cells (PEMFCs) because the diffusion of the gas appeared to be a more important factor than the electrical conduction for better cell performance. Wang et al. [13,14] investigated the effects of the number of flow channel bends, the number of serpentine loops, and the flow channel width ratio on the cell performance of PEMFCs with serpentine flow fields. They particularly probed the effect of the sub-rib convection on cell performances under various channel aspect ratios. According to their results, the sub-rib convection of the serpentine flow field significantly affects the reactant transport efficiency through the GDLs to CLs, and the removal rate of liquid water accumulated underneath the ribs. Manso et al. [15] numerically investigated the influence of the channel cross-section aspect ratio (defined as the ratio height/width) on the performance of a PEMFC with a serpentine flow field design, and analyzed the local current density distributions in the membrane,

* Corresponding author. Tel.: +82 42 860 3501; fax: +82 42 860 3739.
E-mail address: dhpeck@kier.re.kr (D.-H. Peck).
[1] Present address: Fuel Cell Nanomaterials Center, University of Yamanashi, Kofu 400-0021, Japan.

0378-7753/$ – see front matter © 2012 Elsevier B.V. All rights reserved.
doi:10.1016/j.jpowsour.2011.12.055

Nomenclature

a	water activity or effective catalyst area per unit of the total volume ($m^2\ m^{-3}$)
A	area (m^2)
C	molar concentration ($mol\ m^{-3}$)
D_i	mass diffusivity of species i ($m^2\ s^{-1}$)
EW	equivalent weight of a dry membrane ($kg\ mol^{-1}$)
F	Faraday constant (96487 $C\ mol^{-1}$)
i_0	exchange current density ($A\ m^{-2}$)
I	operating current density ($A\ m^{-2}$)
I^{xover}	crossover current density ($A\ m^{-2}$)
j	transfer current density ($A\ m^{-3}$)
j^i	diffusive mass flux of phase i ($kg(m^2\ s)^{-1}$)
J	Leverett function
k_r	relative permeability
K	hydraulic permeability (m^2)
M	molecular weight ($kg\ mol^{-1}$)
m	mass fraction
n	number of electrons in the electrochemical reaction or the diffusivity correction factor
n_c	catalyst coverage coefficient
n_d	electroosmotic drag coefficient
n^{xover}	crossover molar flux ($mol(m^2\ s)^{-1}$)
P	pressure (Pa)
P_c	capillary pressure (Pa)
R_u	universal gas constant (8.314 $J\ (mol\ K)^{-1}$)
s	stoichiometry coefficient in the electrochemical reaction or liquid saturation
S	source term in the transport equation
t	time (s)
T	temperature (K)
$\boldsymbol{u}$	fluid velocity and superficial velocity in a porous medium ($m\ s^{-1}$)
U_o	thermodynamic equilibrium potential (V)
V	volume (m^3)
V_{cell}	cell potential (V)

Greek letters

α	transfer coefficient
δ_i	thickness of component i
ε	volume fraction of the gaseous phase in the porous region
ε_{mc}	volume fraction of the ionomer phase in the CL
γ	advection correction factor
λ	membrane water content ($mol_{H_2O}(mol_{SO_3^-})^{-1}$)
λ^α	relative mobility of phase α
ϕ	phase potential (V)
η	overpotential (V)
θ	contact angle (°)
μ	viscosity ($kg(m\ s)^{-1}$)
ρ	density ($kg\ m^{-3}$)
ρ^{mem}	dry membrane density ($kg\ m^{-3}$)
ν	kinematic viscosity ($m^2\ s^{-1}$)
σ	surface tension ($N\ m^{-1}$) or electronic conductivity ($S\ m^{-1}$)
τ	viscous shear stress, $N\ m^{-2}$, tortuosity
κ	ionic conductivity ($S\ m^{-1}$)
ξ	stoichiometry flow ratio

Superscripts

e	electrolyte
eff	effective value in the porous region
mem	membrane
g	gas
l	liquid
ref	reference value
s	solid
sat	saturation value
xover	crossover

Subscripts

a	anode
avg	average value
BP	bipolar plate
c	cathode
CL	catalyst layer
e	electrolyte
GC	gas channel
GDL	gas diffusion layer
MeOH	methanol
i	species index
in	channel inlet
m	mass equation
mem	membrane
O_2	oxygen
ref	reference value
t	total
s	solid
sat	saturation value
u	momentum equation
w	water
Φ	potential equation
0	standard condition, 298.15 K and 101.3 kPa (1 atm)

velocity distributions, liquid water saturation and hydrogen and oxygen concentrations to understand the channel cross-section aspect ratio effect. These studies demonstrated that flow channel geometry influences the performance of PEMFCs in terms of fuel distribution, mass transport and water removal.

In DMFCs, the flow channel is a critical component for minimizing the mass transport-related issue raised by the two-phase flow of liquid (CH_3OH and H_2O) and gas (CO_2 and air) and for removing a large amount of liquid water on the cathode side, which results from product water by oxygen reduction reaction (ORR) and electro-osmotically dragged water from the anode. Yang et al. [16] experimentally examined the effect of the anode flow field pattern on the performance of a DMFC and reported that both the open ratio and the flow channel length had a significant influence on the cell performance and the pressure drop. Despite these important facts, there have been few papers that dealt with the effect of the flow channel geometry on the performance of DMFCs.

Thus, this paper numerically and experimentally investigates the effects of flow channel geometry on the performance of DMFCs using a single-path serpentine pattern with different channel and rib widths and channel lengths. The through/in-plane transport of methanol and air in DMFCs, the current density distribution and cathode pressure drop are numerically analyzed to examine the effect of the flow channel cross-sectional area on the cell performance for single serpentine DMFCs. In addition, a single cell test, an anode/cathode polarization test, an impedance analysis and measurement of the cathode pressure drop are experimentally conducted to evaluate the characteristics of the different flow channel geometries in DMFCs.

2. Numerical model

2.1. Multi-dimensional, multi-phase fuel cell model and assumptions

The two-phase DMFC model used in this study is based on the multi-phase mixture (M^2) formulation of Wang and Cheng [17]. The present numerical model is developed from the PEFC model developed earlier [18–22] and modified for use in a DMFC system. Utilizing the M^2 formulation to describe two-phase transport in DMFCs, the present model makes the following assumptions:

(1) Laminar flow due to small flow velocities.
(2) Ideal gas mixtures in the gas-phase region.
(3) Isotropic porous media (GDLs and CLs).
(4) Negligible effect of immobile liquid saturation in the porous diffusion medium.

The last assumption is based on the study of Ju [19] in which the effect of immobile liquid saturation is diminished when the diffusion media faces a high liquid saturation level.

2.2. Conservation equations

Under the above assumptions, the two-phase DMFC model is governed by the conservation of mass, momentum, chemical species and charge.

Mass conservation:

$$\nabla \cdot (\rho \vec{u}) = S_m \tag{1}$$

Momentum conservation:
Flow channels (Navier–Stokes equations).

$$\nabla \cdot (\rho \vec{u}\vec{u}) = -\nabla p + \nabla \cdot \tau \tag{2}$$

Porous media (Darcy's equations).

$$\rho \vec{u} = -\frac{K}{\nu} \nabla p \tag{3}$$

Species conservation:
Flow channels and porous media.

$$\nabla \cdot (\gamma_i \rho m_i \vec{u}) = \nabla \cdot [\rho^g D_i^{g,eff} \nabla (m_i^g)] + \nabla \cdot [\rho^l D_i^{l,eff} \nabla (m_i^l)] + \nabla \cdot \left[(m_i^g - m_i^l) \vec{j}^l \right] + S_i \tag{4}$$

Water transport in the membrane.

$$\nabla \cdot \left(\frac{\rho^{mem}}{EW} D_w^{mem} \nabla \lambda \right) M_w - \nabla \cdot \left(n_d \frac{I}{F} \right) M_w + \nabla \cdot \left(\frac{K^{mem}}{\nu^l} \nabla P^l \right) = 0 \tag{5}$$

Charge conservation:

$$\text{Proton transport}: \nabla \cdot (\kappa^{eff} \nabla \Phi_e) + S_\Phi = 0. \tag{6}$$

$$\text{Electron transport}: \nabla \cdot (\sigma^{eff} \nabla \Phi_s) - S_\Phi = 0 \tag{7}$$

2.3. Two-phase transport properties

Generally, two-phase mixture properties are expressed as functions of s, the volume fraction of pores occupied by the liquid phase, and $(1-s)$, the volume fraction of pores occupied by the gaseous phase. The different mixture properties are defined as follows [17].

Mixture density:

$$\rho = \rho^l s + \rho^g (1-s). \tag{8}$$

In Eq. (8), ρ^g is the gas mixture density described by the ideal gas law; it varies with the species composition (the mass fractions, $\{m_i^g\}$). That is,

$$\rho^g = \left(\frac{P}{R_u T} \right) \frac{1}{\sum_i m_i^g / M_i}. \tag{9}$$

Mixture velocity:

$$\vec{u} = \frac{\rho^l \vec{u}^l + \rho^g \vec{u}^g}{\rho}. \tag{10}$$

Species mass fraction:

$$m_i = \frac{\rho^l s m_i^l + \rho^g (1-s) m_i^g}{\rho}. \tag{11}$$

Relative permeability:

$$k_r^l = s^4, \tag{12a}$$

$$k_r^g = (1-s)^4. \tag{12b}$$

Kinematic viscosity:

$$\nu = \left(\frac{k_r^l}{\nu^l} + \frac{k_r^g}{\nu^g} \right)^{-1}. \tag{13}$$

In Eq. (13), ν^g is the kinematic viscosity of the gas mixture that varies with the gas composition [23]:

$$\nu^g = \frac{\mu^g}{\rho^g} = \frac{1}{\rho^g} \sum_{i=1}^{n} \frac{x_i \mu_i}{\sum_{j=1}^{n} x_j \Phi_{ij}}, \quad \text{where}$$

$$\Phi_{ij} = \frac{1}{\sqrt{8}} \left(1 + \frac{M_i}{M_j} \right)^{-1/2} \left[1 + \left(\frac{\mu_i}{\mu_j} \right)^{1/2} \left(\frac{M_j}{M_i} \right)^{1/4} \right]^2 \tag{14}$$

and

$$\mu_i \ (\text{N s m}^{-2}) = \begin{cases} \mu_w = 0.00584 \times 10^{-6} T^{1.29} \\ \mu_{N_2} = 0.237 \times 10^{-6} T^{0.76} \\ \mu_{O_2} = 0.246 \times 10^{-6} T^{0.78} \end{cases}, T \text{ in K.}$$

Relative mobility:

$$\lambda^l = \frac{k_r^l}{\nu^l} \nu, \tag{15a}$$

$$\lambda^g = 1 - \lambda^l. \tag{15b}$$

The species diffusivity in the gas mixture, D_i^g, in the first term in the right-hand side of Eq. (4) is defined as follows in order that the cumulative interspecies diffusion within the gaseous phase is equal to zero [23].

$$D_i^g = \frac{1 - x_i}{\sum_{\substack{j \\ j \neq i}}^{j=n} x_j / D_{i,j}},$$

$$\text{where} \quad D_{i,j} = \frac{1.013 \times 10^{-7} \cdot T^{1.75}}{p \cdot \left(\chi_i^{1/3} + \chi_j^{1/3} \right)^2} \cdot \left(\frac{1}{M_i} + \frac{1}{M_j} \right)^{1/2}, \tag{16}$$

$$\chi_w = 12.7, \quad \chi_{N_2} = 17.9, \quad \chi_{O_2} = 16.6$$

Note that the gaseous diffusive transport for a porous medium can be controlled by the Knudsen diffusion effect due to molecule-to-wall collision as well as the molecular diffusion which is caused by inter-molecular collision, as described in Eq. (16). The Knudsen diffusion coefficient can be computed according to the kinetic theory of gases as follows.

$$D_i^K = \frac{2}{3} \left(\frac{8 R_u T}{\pi M_i} \right)^{1/2} r_p \tag{17}$$

The effective diffusivity of species i in the gas mixture is then obtained by combining both the molecular and Knudsen diffusion effects with the effects of the porosity and tortuosity of the porous medium using Bruggeman's correlation.

$$D_i^{g,eff} = [\varepsilon(1-s)]^{\tau}\left(\frac{1}{D_i^g}+\frac{1}{D_i^K}\right)^{-1} \tag{18}$$

The effective diffusivity of species i in the liquid phase is obtained as,

$$D_i^{l,eff} = [\varepsilon s]^{\tau} D_i^l \tag{19}$$

Assuming the vapor–liquid equilibrium of methanol on the anode side and invoking Henry's law, the transportation equation for methanol can be written as,

$$\nabla\cdot(\gamma_{MeOH}\rho m_{MeOH}\vec{u}) = \begin{bmatrix} \nabla\cdot\left[\rho^l\left(D_{MeOH}^{l,eff}+\dfrac{D_{MeOH}^{g,eff}}{k_H}\right)\nabla(m_{MeOH}^l)\right] \\ -\nabla\cdot\left[\left(1-\dfrac{\rho^l}{\rho^g k_H}\right)m_{MeOH}^l\vec{j}^l\right]+S_{MeOH}\end{bmatrix} \tag{20}$$

where $D_{MeOH}^{l,eff} = (\varepsilon s)^{\tau} D_{MeOH}^l$
$D_{MeOH}^{g,eff} = [\varepsilon(1-s)]^{\tau} D_{MeOH}^g$
$S_{MeOH} = -\dfrac{j}{6F} - \dfrac{j^{xover}}{6F}$ Anode catalyst layer

where Henry's constant, k_H, is defined as the ratio between the methanol concentration in the liquid and gas phases and is expressed as a function of temperature, i.e.,

$$k_H = \frac{C_{MeOH}^l}{C_{MeOH}^g} = k_H^0 e^{-[(\Delta H_{sol}/R)((1/T)-(1/T_0))]RT}, \tag{21}$$

where k_H^0 refers to Henry's constant at the reference state of $T_0 = 298.15$ K and ΔH_{sol} refers to the enthalpy of the solution. It is seen that the effective liquid and gas diffusivities in the two-phase region are functions of both of the porosity, ε, and the liquid saturation, s.

Assuming complete consumption of methanol at the cathode catalyst layer after it crosses over the membrane from the anode to cathode, the methanol flux driven by electro-osmotic drag (EOD) and diffusion can be written as:

$$\frac{j^{xover}}{6F} = \nabla.\left(n_{d,MeOH}\frac{i_e}{F}\right) + \nabla.\left(D_{MeOH}^{mem}\frac{C_{MeOH}^l\big|_{cata}}{\delta_{mem}}\right) \tag{22}$$

where $n_{d,MeOH}$ denotes the EOD coefficient for methanol which is a function of EOD coefficient of water, and the ratio of the methanol to water concentrations in the anode CL. That is,

$$n_{d,MeOH} = n_{d,w}\left.\frac{C_{MeOH}^l}{C_w^l}\right|_{aCL} \tag{23}$$

The diffusive mass flux of the liquid phase, $\vec{j}^l$, which is shown in the third term in the right-hand side of Eq. (4), is expressed as a function of the capillary pressure, P_c, such that [17]:

$$\vec{j}^l = \rho^l\vec{u}^l - \lambda^l\rho\vec{u} = \frac{K}{\nu}\lambda^l\lambda^g\nabla P_c \tag{24}$$

In Eq. (24), the correlations of the capillary pressure, P_c, and the Leverett function, $J(s)$, are found as below.

$$P_c = P^g - P^l = \sigma\cos\theta\left(\frac{\varepsilon}{K}\right)^{1/2}J(s), \tag{25}$$

$$J(s) = \begin{cases} 1.417(1-s)-2.120(1-s)^2+1.263(1-s)^3 & \text{if } \theta_c < 90^\circ \\ 1.417s-2.120s^2+1.263s^3 & \text{if } \theta_c > 90^\circ \end{cases} \tag{26}$$

The term in the left-hand side of the species equation represents the advective term, in which the advection correction factor, γ_i, is given by Wang and Cheng [17].

$$\gamma_i = \frac{\rho(\lambda^l m_i^l + \lambda^g m_i^g)}{(s\rho^l m_i^l + (1-s)\rho^g m_i^g)} \tag{27}$$

The liquid saturation, s, can be calculated via,

$$s = \frac{C_w - C_{w,sat}^g}{C_w^l - C_{w,sat}^g} \tag{28}$$

where liquid water concentration, C_w^l, can be calculated by assuming the vapor–liquid equilibrium of methanol as follows:

$$\begin{aligned} C_{MeOH}^l &= \frac{C_{MeOH}}{[s+((1-s)/k_H)]} \\ m_{MeOH}^l &= \frac{C_{MeOH}.M_{MeOH}}{[(s+((1-s)/k_H))\rho^l]} \\ C_w^l &= \frac{(1-m_{MeOH}^l)\rho^l}{M_w}. \end{aligned} \tag{29}$$

The transport properties of electrolytes are correlated with the water content of the membrane, λ, which, in turn, is a function of the water activity, a, as follows [24].

$$a = \frac{C_w^g R_u T}{P_{sat}} \tag{30}$$

$$\lambda = \begin{cases} \lambda^g = 0.043 + 17.81a - 39.85a^2 + 36.0a^3 & \text{for } 0 < a \le 1 \\ \lambda^l = 22 \end{cases} \tag{31}$$

The electro-osmotic drag coefficient, n_d, the proton conductivity in the membrane, κ, and the water diffusion coefficient in the membrane, D_w^{mem}, are given by Springer et al. [24].

$$n_{d,w} = \frac{2.5\lambda}{22} \tag{32}$$

$$\kappa = (0.5139\lambda - 0.326)\exp\left[1268\left(\frac{1}{303}-\frac{1}{T}\right)\right] \tag{33}$$

$$D_w^{mem} = \begin{cases} 2.692661843\times10^{-10} & \text{for } \lambda \le 2 \\ \{0.87(3-\lambda)+2.95(\lambda-2)\}\times10^{-10}\cdot e^{(7.9728-(2416/T))} & \text{for } 2 < \lambda \le 3 \\ \{2.95(4-\lambda)+1.642454(\lambda-3)\}\times10^{-10}\cdot e^{(7.9728-(2416/T))} & \text{for } 3 < \lambda \le 4 \\ (2.563-0.33\lambda+0.0264\lambda^2-0.000671\lambda^3)\times10^{-10}\cdot e^{(7.9728-(2416/T))} & \text{for } 4 > \lambda \end{cases} \tag{34}$$

2.4. Electrochemical reactions and source terms

In the above conservation equations, namely, (1)–(7), S_m, S_i and S_Φ, which are listed in Table 1, denote the corresponding source/sink terms for mass, species and charge. These source terms result from the electrochemical reactions: the methanol oxidation reaction (MOR) in the anode CL and the ORR in the cathode CL. These electrochemical reactions are represented by kinetic expressions as follows.

MOR in the anode CL [25–27]:

$$j = \frac{aj_{0,a}^{ref}\,C_{MeOH}^l\big|_{cata}\exp((\alpha_a F/RT)\eta_a)}{C_{MeOH}^l\big|_{cata} + K_j\exp((\alpha_a F/RT)\eta_a)} \tag{43}$$

ORR in the cathode CL:

$$j_c = -(1-s)^{n_c}ai_{o,c}^{ref}\left(\frac{C_{O_2}}{C_{O_2,ref}}\right)^{3/4}\exp\left(-\frac{\alpha_c}{R_u T}F\eta\right) \tag{44}$$

where

$$j_c = j + j^{xover} \tag{45}$$

Table 1
Two-phase steady-state DMFC model: source/sink terms.

Source terms	Anode catalyst layer	Cathode catalyst layer
MeOH	$S_{MeOH} = M_{MeOH}\left[-\frac{j_a}{6F} - \nabla\cdot\left(n_{d,MeOH}\frac{i_e}{F}\right) - \nabla\cdot\left(D^{mem}_{MeOH}\frac{C^{l}_{MeOH}\big\vert_{cata}}{\delta_{mem}}\right)\right]$ (35)	
O_2		$S_{O_2} = M_{O_2}\left[\frac{j_c}{4F} - \frac{3}{2}\frac{n^{xover}_{MeOH}}{\delta_{CL}}\right]$ (36)
H_2O	$S_w = M_w\left[-\frac{j_a}{6F} - \nabla\left(n_{d,w}\frac{i_e}{F}\right) - \nabla\cdot\left(D^{mem}_{w}\frac{\rho^{mem}}{EW}\nabla\lambda\right)\right]$ (37a)	$S_w = M_w\left[\nabla\cdot\left(D^{mem}_{w}\frac{\rho^{mem}}{EW}\nabla\lambda\right) + \nabla\left(n_{d,w}\frac{i_e}{F}\right) - \frac{j_c}{2F} + 2\frac{n^{xover}_{MeOH}}{\delta_{CL}}\right]$ (37b)
Mass	$S_m = \sum_k S_k =$	$S_m = \sum_k S_k =$
	$M_{MeOH}\left[-\frac{j_a}{6F} - \nabla\cdot\left(n_{d,MeOH}\frac{i_e}{F}\right) - \nabla\cdot\left(D^{mem}_{MeOH}\frac{C^{l}_{MeOH}\big\vert_{cata}}{\delta_{mem}}\right)\right] +$	$M_{O_2}\frac{j_c}{4F} - M_w\frac{j_c}{2F} + M_w\left[\nabla\cdot\left(D^{mem}_{w}\frac{\rho^{mem}}{EW}\nabla\lambda\right) + \nabla\left(n_d\frac{i_e}{F}\right)\right] + \frac{M_{MeOH}n^{xover}_{MeOH}}{\delta_{CL}}$ (38b)
	$M_w\left[-\frac{j_a}{6F} - \nabla\cdot\left(D^{mem}_{w}\frac{\rho^{mem}}{EW}\nabla\lambda\right) - \nabla\left(n_d\frac{i_e}{F}\right)\right]$ (38a)	
Charge	$S_\phi = j$ (39a)	$S_\phi = -j_c + j^{xover}$ (39b)
Electro-chemical reactions	$\sum_k s_i M_i^z = ne^-$, where $\begin{cases} M_i \equiv \text{chemical formula of species } i \\ s_i \equiv \text{stoichiometry coefficient} \\ n \equiv \text{number of electrons transferred} \end{cases}$	(40)
	Methanol oxidation reaction (MOR) in anode side : $CH_3OH + H_2O = CO_2 + 6H^+ + 6e^-$	(41)
	Oxygen reduction reaction (ORR) in cathode side : $3/2O_2 + 6H^+ + 6e^- = 3H_2O$	(42)

In Eq. (44), $(1-s)^{n_c}$ approximates the effect of the decreasing number of electrochemically active catalyst sites due to the presence of water in the CLs.

The surface overpotential in Eqs. (43) and (44) is defined by:

MOR in the anode CL:

$$\eta = \varphi_s - \varphi_e \tag{46}$$

ORR in the cathode CL:

$$\eta = \varphi_s - \varphi_e - U_0 \tag{47}$$

In Eq. (47), the thermodynamic equilibrium potential between the cathode and anode can be written as follows.

$$U_0 = 1.23 - 0.9\times10^{-3}(T - 298.15) \tag{48}$$

The temperature dependence of the MOR kinetics [28] and ORR kinetics [29] are expressed as follows.

$$ai^{ref}_{0,a}(T) = ai^{ref}_{0,a}(353K)\cdot\exp\left[-\frac{35570}{R}\left(\frac{1}{T} - \frac{1}{353.15}\right)\right] \tag{49a}$$

$$ai^{ref}_{0,c}(T) = ai^{ref}_{0,c}(353K)\cdot\exp\left[-\frac{73200}{R}\left(\frac{1}{T} - \frac{1}{353.15}\right)\right] \tag{49b}$$

2.5. Boundary conditions

The inlet velocities in the anode and cathode gas channels can be expressed as functions of the anode and cathode stoichiometric ratios (ξ_a and ξ_c), respectively, the DMFC operating current density (I), the cross-sectional areas of the anode and cathode gas channels (A_a and A_c), respectively, and the inlet concentration of methanol and oxygen, which are functions of the anode/cathode inlet pressure, temperature, and humidity.

$$u_{in,a} = \frac{\xi_a(I/6F)A_{mem}}{C_{MeOH}A_a} \quad \text{and} \quad u_{in,c} = \frac{\xi_c(I/4F)A_{mem}}{C_{O_2}A_c} \tag{50}$$

In addition, the isothermal boundary condition (60 °C in this study) and the constant current boundary condition are applied to the bipolar plate's outer surfaces, whereas no-slip and impermeable velocity condition and no-flux condition are applied to the outer faces for the velocity and species calculations.

2.6. Flow channel geometry and numerical procedures

The DMFC model described above was implemented with a commercial computational fluid dynamics (CFD) package, STAR-CD, based on its user-coding capability [30].

To investigate the effects of the flow channel geometry on the performance of DMFCs, single-path serpentine patterns with an active area of 9 cm^2 (3 cm × 3 cm) was conducted for the numerical analyses. The flow channel geometries were designed with different channel and rib widths, channel lengths, cross-sectional area ratios and number of U-turns, as shown in Fig. 1. Numerical meshes were generated for four different geometries with a single-path serpentine flow field. The flow channels had channel widths of 0.7, 1.0 and 1.5 mm, rib widths of 0.5 and 1.0 mm, and channel lengths of 450, 570 and 750 mm; all of the channels had a depth of 1.0 mm. The detailed physical geometries of the single-path serpentine are summarized in Table 2. The flow field designs with channel/rib widths of 0.7/0.5 mm, 1.0/0.5 mm, 1.5/0.5 mm and 1.0/1.0 mm are denoted as F1-, F2-, F3- and F4-type channel, respectively.

Fig. 2 shows the mesh configuration of the F2-type geometry. In the present work, the computational domain of a DMFC consists of seven sub regions, namely, flow channels, backing layers (BL) and CLs in both anode and cathode sides, and a membrane. Roughly 1.2 million cells were applied for each of the four geometries and it required 16 s per iteration on a 8-PC cluster (Intel® Core™ i7 processor 2.53 GHz).

Table 2
Channel name and physical geometries of the flow field patterns with different channel and rib widths.

Channel name	Channel/rib width (mm)	Channel length (mm)	Channel area (mm^2)	Rib area (mm^2)	Percentages of rib area in active electrode area (%)
F1	0.7/0.5	750	525	360	40.7
F2	1.0/0.5	570	570	270	32.1
F3	1.5/0.5	450	675	210	23.7
F4	1.0/1.0	450	450	420	48.3

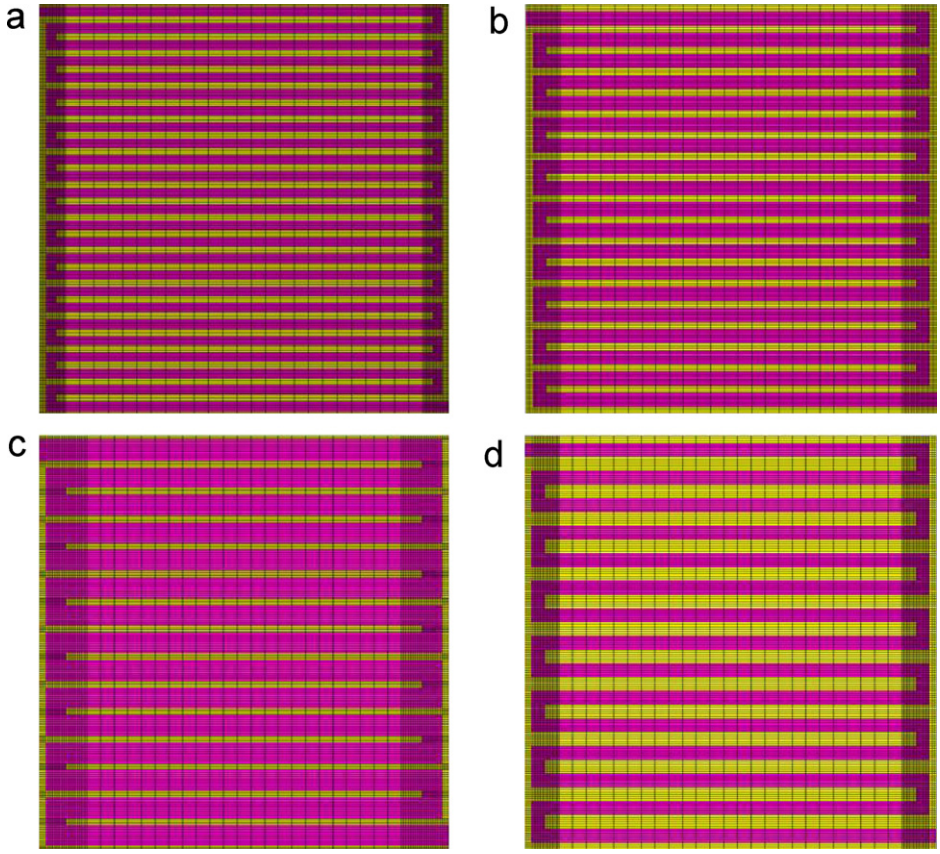

Fig. 1. Flow channel geometries: (a) F1-, (b) F2-, (c) F3- and (d) F4-type.

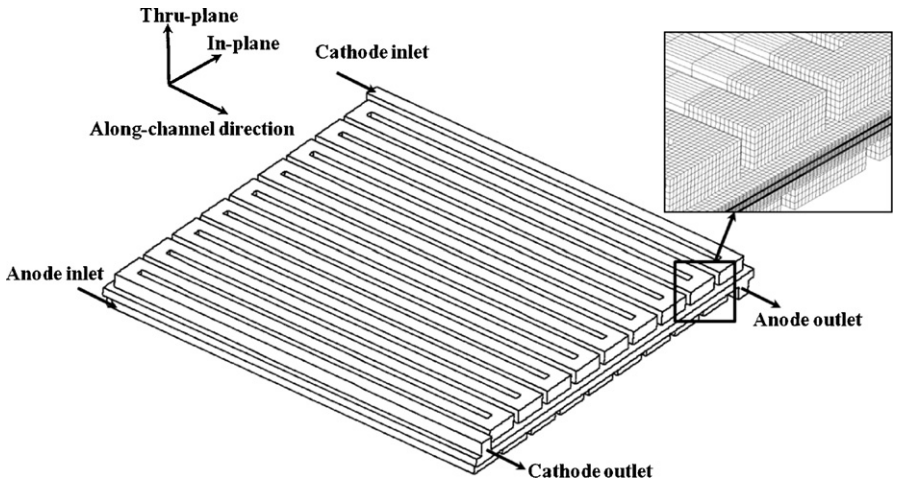

Fig. 2. Mesh configuration of the F2-type geometry.

3. Experimental

3.1. MEA preparation

The MEA with an active electrode area of 9.0 cm^2 was fabricated using commercial Nafion 115 as the membrane, PtRu/C (HISPEC 12100, Johnson Matthey Fuel Cells, UK) as the anode catalyst, and Pt/C (HISPEC 13100, Johnson Matthey Fuel Cells, UK) as the cathode catalyst [31]. The catalysts, Nafion solution (10 wt%, DuPont, USA), distilled water, isopropyl alcohol, and 1-propanol were mixed to make the electrode catalyst slurry, and the mixture was homogenized with an ultrasonic processor (Hielscher, UP100H, Germany). The mixture was then stirred with a magnetic stirring system to prepare the appropriate catalyst slurry. The catalyst slurry was painted onto the GDL using a brushing method. The GDL for the anode and the cathode were carbon paper (TGP-H-060, Toray, Japan) that was treated with 5 wt% PTFE and a carbon sheet (GDL 25BC, SGL Carbon, Germany), respectively. The loading of the catalysts was 2 mg cm^{-2} PtRu for the anode and 2 mg cm^{-2} Pt for the cathode. The electrode layers and Nafion membrane were hot pressed using a laboratory press (Carver, Model M, USA). The hot pressing of the MEAs was performed at a temperature of 150 and a pressing pressure of 50 kg cm^{-2} for 60 s.

3.2. Characteristics analysis of flow channel geometry

To investigate the effects of the flow channel geometry on the performance of DMFCs, the single cells with the same active electrode area of 9.0 cm^2, GDL, CL, and proton exchange membrane was tested using an electrochemical test system (Won-A Tech., Korea). A solution of 1 M methanol solution was fed into the anode at a flow rate of $\lambda = 2.5$ and air was supplied to the cathode at a flow rate of $\lambda = 3$ under ambient pressure. The anode polarization of the cells was also measured under the same conditions as the single cell test; however, to create a dynamic hydrogen electrode (DHE) in this case, hydrogen (H_2) gas was supplied to the cathode at a flow rate of 10 ml min^{-1}.

The ohmic resistance and electrochemical impedance spectra of the single cells during the electrochemical reaction can be observed using an electrochemical analysis instrument (Zahner, IM6&IM6eX, Germany). Nyquist plots of the impedance were recorded under galvanostatic conditions of 100 and 400 mA cm^{-2}. All anode impedances were measured between the anode and a DHE in the complete fuel cell, whereas the impedance of a complete cell was obtained using a DMFC single cell system (methanol/air). The frequency range varied from 3 mHz to 10 kHz and the amplitude of the AC voltage was 10 mV.

The analytical pressure drop of the different flow channel geometries was calculated by the following Darcy–Weisbach equation [32],

$$\Delta P = f\left(\frac{L}{D_h}\right)\rho\left(\frac{v^2}{2}\right) \tag{51}$$

Here, ΔP is the pressure loss due to friction, f is the friction factor, L is the channel length (m), D_h is the hydraulic diameter (m), ρ is the fluid density (air = 1.23 kg m^{-3}), and v is the velocity of the flow (m s^{-1}). For the laminar flow of Re < 2000, the friction factor (f) is defined as Eq. (52),

$$f = \frac{64}{\mathrm{Re}} \tag{52}$$

where Re is the Reynolds number.

Re is defined as the following Eq. (53),

$$\mathrm{Re} = \frac{\rho v D_h}{\mu} \tag{53}$$

where μ is the viscosity of the fluid (kg m^{-1} s^{-1}) (air = 1.81×10^{-5} kg m^{-1} s^{-1}).

For a rectangular channel with w_c as the width and d_c as the depth, hydraulic diameter (D_h) is defined as Eq. (54):

$$D_h = \frac{2w_c.d_c}{w_c + d_c} \tag{54}$$

D_h and v as well as Re values for the calculation of the analytical pressure drop of the different flow channel geometries are represented in Table 3. The experimental pressure drop in the flow channels was measured at each current density from 100 to 500 mA cm^{-2} under a flow rate of $\lambda = 3$ using a nanometer that was installed at the inlet of the cathode.

4. Results and discussion

In this study, the presented two-phase DMFC model was applied to a single-path serpentine channel cell, as shown in Fig. 1 with its mesh configuration. The methanol solution and air were fed into the anode and cathode inlets, respectively, under the counter-flow configuration. The individual cell properties and operating conditions are listed in Table 4, and the relevant physical and transport properties are given in Table 5. Using the cell configuration, the cell properties, the operating conditions and the physical properties, a numerical study was conducted to investigate the effects of the flow channel cross-sectional area on the performance of serpentine DMFCs.

In general, DMFCs supply methanol and air through the flow field channel to the GDL and the CL, and the produced CO_2 gas or H_2O from the cell is reversely transported out. This two-phase flow behavior of DMFCs significantly affects the mass transport of reactants (methanol and air) and the removal of products (CO_2 gas or H_2O) in the anode and cathode side, and thereby it determines the cell performance of DMFCs [36]. During the fuel cell operation, the methanol and air transport processes in DMFCs was confirmed through the methanol concentration in the anode and the air concentration in the cathode.

4.1. Effect of the flow channel geometry on performance of DMFCs

Fig. 3 shows the experimentally measured and numerically simulated polarization curves of the single cells using the different flow channel geometries listed in Table 2. Both the numerical and experimental results revealed that these cells exhibit the different performances with the flow channel geometries employed in each cell. According to the experimental results, F2-type flow channel is superior to other type flow channels. Based on the same rib width of 0.5 mm, the F2-type flow channel (channel width: 1.0 mm, rib width: 0.5 mm) had the highest maximum current density of 670 mA cm^{-2} at 0.2 V and the highest maximum power density of 152 mW cm^{-2} (550 mA cm^{-2} @ 0.277 V), whereas the F1-type flow channel (channel width: 0.7 mm, rib width: 0.5 mm) and F3-type flow channel (channel width: 1.5 mm, rib width: 0.5 mm) had a maximum current density of 580 and 540 mA cm^{-2} at 0.2 V and a maximum power density of 132 mW cm^{-2} (480 mA cm^{-2} @ 0.276 V) and 131 mW cm^{-2} (450 mA cm^{-2} @ 0.289 V), respectively. In terms of the constant channel width (1.0 mm), the F2-type flow channel with a narrow rib width (channel width: 1.0 mm, rib width: 0.5 mm) showed much better performance than the broad rib width case, i.e., the F4-type flow channel (channel width: 1.0 mm, rib width: 1.0 mm). The experimental trend agrees well with the previous study on PEMFC [12] in which a narrow rib width of 0.5 mm brought about the performance improvement. These results show the strong effect of the flow channel geometry on the performance of DMFCs. In addition, these experimental trends were correctly captured by the present DMFC model. To

Table 3
D_H, ν and Re values for calculation of the theoretical pressure drop (ΔP) of the different flow channel geometries calculated by Darcy–Weisbach equation (50) according to current density (stoichiometry $\lambda = 3$).

Channel name	D_H (mm)	ν and Re values (ν/Re) according to current density				
		100 mA cm^{-2}	200 mA cm^{-2}	300 mA cm^{-2}	400 mA cm^{-2}	500 mA cm^{-2}
F1	0.82	1.32/74	2.60/146	3.93/221	5.24/295	6.52/376
F2	1.0	0.92/63	1.82/124	2.75/188	3.67/251	4.57/312
F3	1.2	0.61/50	1.21/99	1.83/150	2.44/200	3.04/250
F4	1.0	0.92/63	1.82/124	2.75/188	3.67/251	4.57/312

Table 4
Cell properties and operating conditions.

Description	Value
Thickness of anode GDL	190×10^{-6} m
Thickness of anode CL	30×10^{-6} m
Thickness of cathode GDL	235×10^{-6} m
Thickness of cathode CL	30×10^{-6} m
Thickness of membrane	127×10^{-6} m
Thickness of bipolar plate	2×10^{-3} m
Porosity of GDLs, ε_{GDL}	0.7
Porosity of CLs, ε_{CL}	0.7
Volume fraction of ionomer in CLs, ε_{mc}	0.23
Permeability of GDLs, K_{GDL}	1.0×10^{-12} m^2
Permeability of GDLs, K_{CL}	1.0×10^{-12} m^2
Hydraulic permeability of a membrane, K_{mem}	5.0×10^{-19} m^2
Contact angle of GDLs and CLs, θ	92°
Anode stoichiometry	2.5
Cathode stoichiometry	3.0
Cell operating temperature	60 °C
Anode/cathode inlet pressure	Atmospheric
Inlet methanol concentration	1000 mol m^{-3}

Table 5
Physical and transport properties in the individual cell.

Description	Value	Ref.
Reference exchange current of anode, $ai^{ref}_{0,a}$	1.2×10^6 A m^{-3}	
Reference exchange current of cathode, $ai^{ref}_{0,c}$	1.407×10^3 A m^{-3}	
Reference oxygen molar concentration, $c_{O_2,ref}$	7.68 $mol\,m^{-3}$	
Anodic transfer coefficients for MOR, α_a	0.5	
Cathodic transfer coefficient for the ORR, α_c	0.8	
Activation energy for MOR, E_{aa}	35570 J kg^{-1}	Wang and Wang [28]
Activation energy for ORR, E_{ac}	73200 J kg^{-1}	Parthasarathy et al. [29]
Dry membrane density, ρ^{mem}	2000 kg m^{-3}	
Equivalent weight of electrolyte in the membrane, EW	1.1 kg mol^{-1}	
Faraday constant, F	96487 C mol^{-1}	
Universal gas constant, R_u	8.314 J(mol K)$^{-1}$	
Surface tension, σ	0.0625 N m^{-1}	
Liquid water viscosity, μ^l	3.5×10^{-4} (N s)m^{-2}	
Diffusion coefficient of methanol in liquid, D^l_{MeOH}	$10^{-5.4163-999.778/T}$ m^2 s^{-1}	Wang and Wang [28]
Diffusion coefficient of methanol in gas, D^g_{MeOH}	$\begin{pmatrix} -6.954 \times 10^{-2} + 4.5986 \times 10^{-4} T \\ +9.4979 \times 10^{-7} T^2 \end{pmatrix} \times 10^{-4}$ m^2 s^{-1}	Yaws [33]
Diffusion coefficient of oxygen in gas, D^g_w	$1.775 \times 10^{-5}(T/273)^{1.823}(1.013 \times 10^5/p)$ m^2 s^{-1}	Cussler [34]
Diffusion coefficient of water in gas, D^g_w	$2.56 \times 10^{-5}(T/307)^{2.334}(1.013 \times 10^5/p)$ m^2 s^{-1}	Cussler [34]
Electro-osmotic drag coefficient of water, $n_{d,w}$	2.5	Ren et al. [35]

elucidate this phenomenon, it should be noted that the performance of the cells in the low current density regions was hardly affected by the channel and rib width, whereas the cell performance in the high current density regions was significantly dominated by the channel/rib cross section geometries. This could be ascribed to the differences in electrical conduction of the cells with different rib areas, which influenced the ohmic loss in the IR region or it could be caused by the difference in the mass transport capability of the flow channel geometries, which affected the access of the reactant gas (methanol and air) to the electrode layer as well as the product removal (H_2O and CO_2) from the electrode layer. It is, however, very difficult to elicit a conclusion with only the polarization curves. Thus, the numerical and experimental studies were chosen to accompany the polarization curves in order to examine any effects of the flow channel geometries on the performance of DMFCs.

Fig. 4 illustrates the simulated current density distributions (A m^{-2}) over the membrane at the operating current density of 400 mA cm^{-2} with F1–F4 type channel geometries. These results exhibit a wealth of current non-uniformity features over the entire cell of 9 cm^2. First, it is found that the current density distribution is mainly controlled by the effect of oxygen depletion along the cathode downstream rather than methanol depletion along the anode flow path. Second, the local current density near the flow channels is higher than near the ribs, implying a strong rib effect. Comparing Fig. 4(b) and Fig. 4(d), a small current density gradient between the channel and rib regions is observed in the F2-type flow channel (Fig. 4(b)) owing to its narrower rib width (0.5 mm).

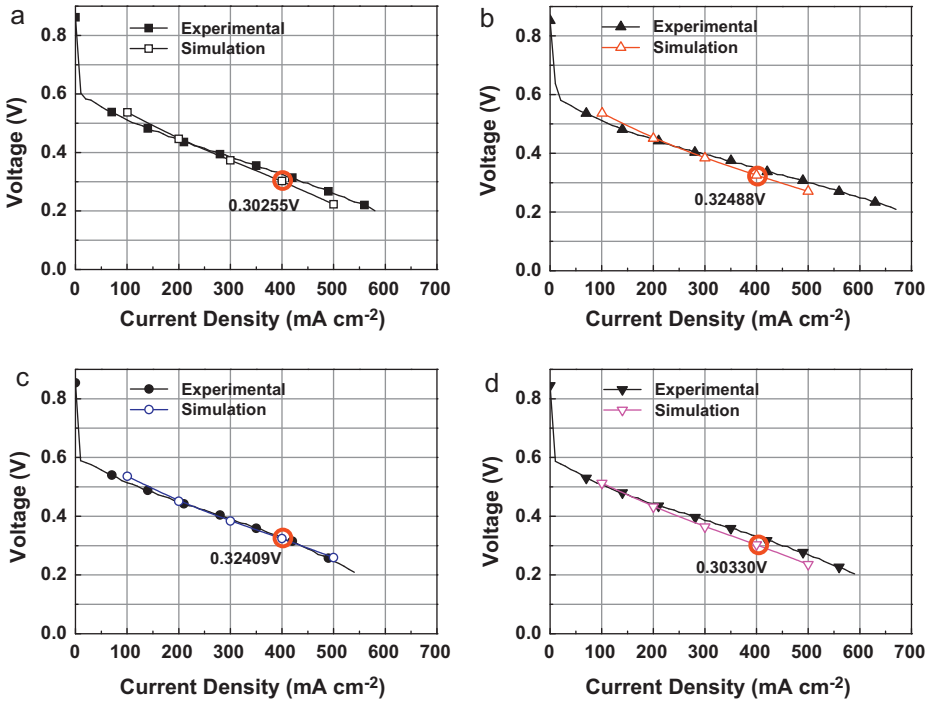

Fig. 3. Experimental and simulated polarization curves for (a) Fl-, (b) F2-, (c) F3- and (d) F4-types of geometries.

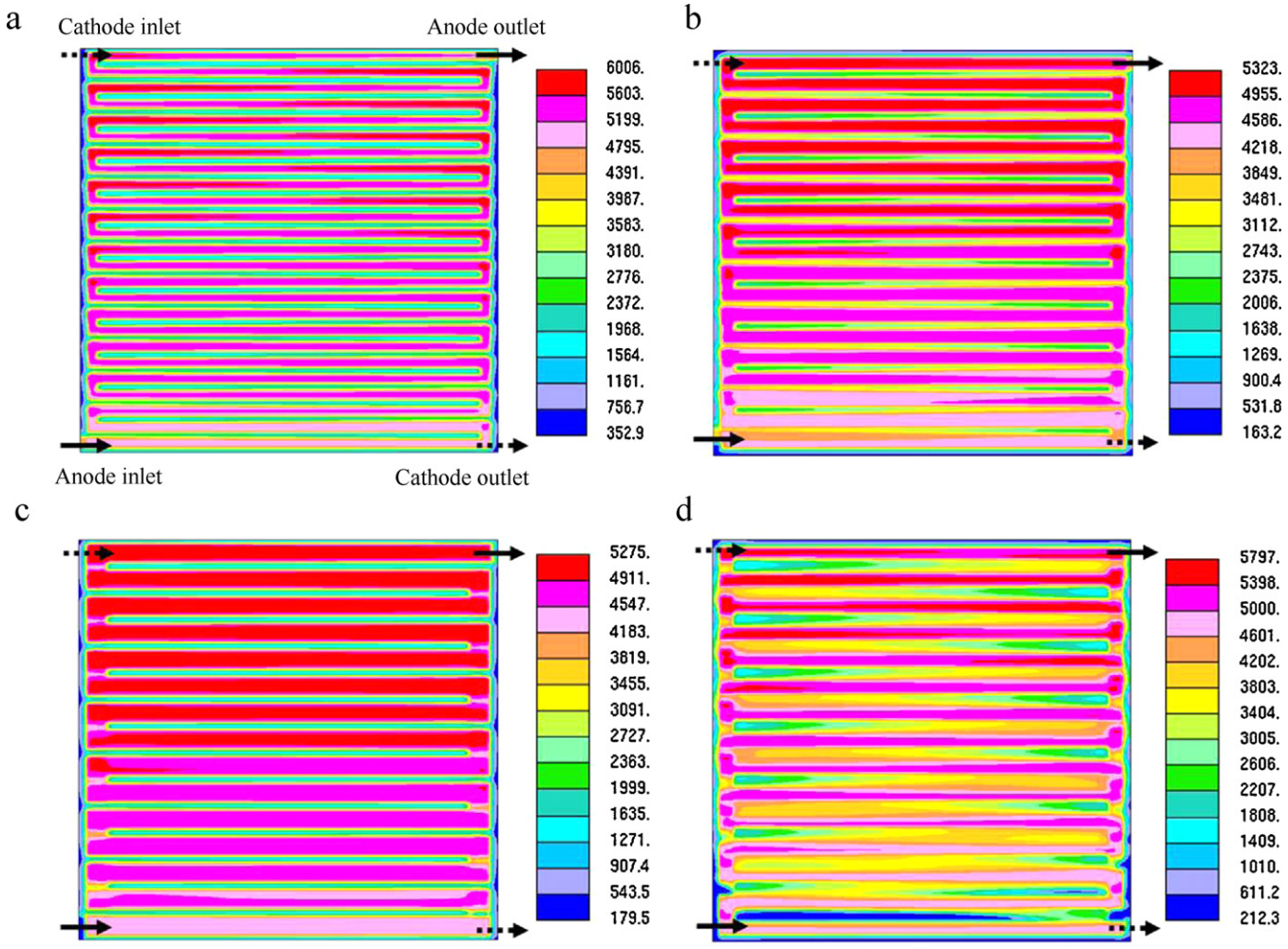

Fig. 4. Simulated current density contours in the membrane for (a) Fl-, (b) F2-, (c) F3- and (d) F4-types of geometries.

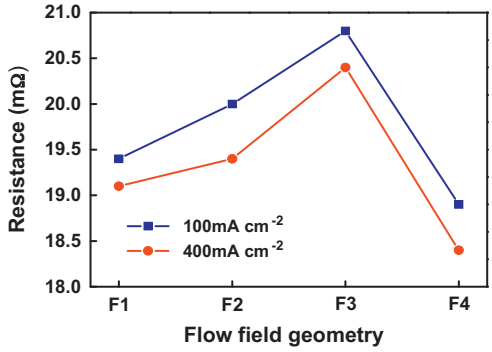

Fig. 5. Experimental ohmic resistance of the cells with different percentages of rib area at current densities of 100 mA cm^{-2} and 400 mA cm^{-2}.

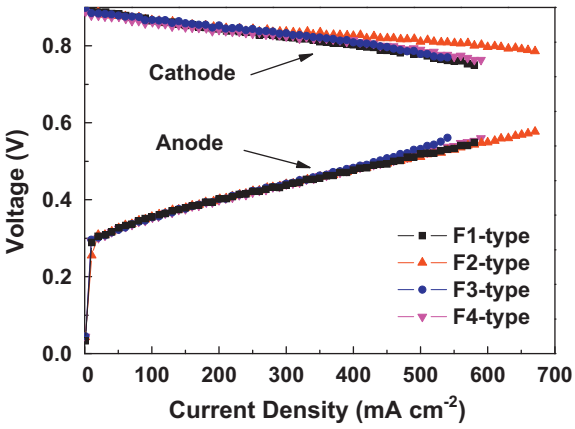

Fig. 6. Experimental anode and cathode polarization curves of the cells using the different flow channel geometries at an operating temperature of 60 °C.

On the other hand, the broad rib of the flow channel (F4-type flow channel) created a little longer convection route and thereby led to insufficient sub-rib convection of methanol and air. This result indicates that the narrow rib of the flow channel is advantageous to the two-phase transport under the ribs, leading to the increase of the cell performance. Based on the same rib width of 0.5 mm, a comparison of Fig. 4(a), Fig. 4(b) and Fig. 4(c) indicates that the flow channel width (F1-type: 0.7 mm, F2-type: 1.0 mm, F3-type: 1.5 mm) is another factor affecting current density distribution in the membrane. The flow channel width determines the direct contact area between the fuels and the GDLs, and the broad channel results in less reactant transport loss under similar active electrode areas (F1-type: 885 mm^2, F2-type: 840 mm^2, F3-type: 870 mm^2). Therefore, F3-type with the broader channel width shows better current density distribution in the flow channel than F1-type and F2-type with the narrower channel width. However, due to the smaller percentage of rib area in F3-type, i.e. 23.7% and the resultant higher electronic resistance, the F2-type flow channel shows better current density distribution than the F3-type flow channel.

These results verify that the narrow rib width and the suitable channel/rib aspect ratio (here, the channel/rib aspect ratio is 2:1) need to increase the cell performance of serpentine DMFCs.

4.2. Parameters of the flow channel geometry on performance of DMFCs

The ohmic resistance of these cells with the different rib areas was experimentally measured at a low current density (100 mA cm^{-2}) and a high current density (400 mA cm^{-2}), respectively, as presented in Fig. 5. Increase of the rib area resulted in a linear decrease of the ohmic resistance of the cells (F1-type: 360 mm^2, F2-type: 270 mm^2, F3-type: 210 mm^2, F4-type: 420 mm^2). This result originates from the difference in current passage areas, which are formed by contact between a rib and a GDL. It should be noted, however, that the difference in the ohmic

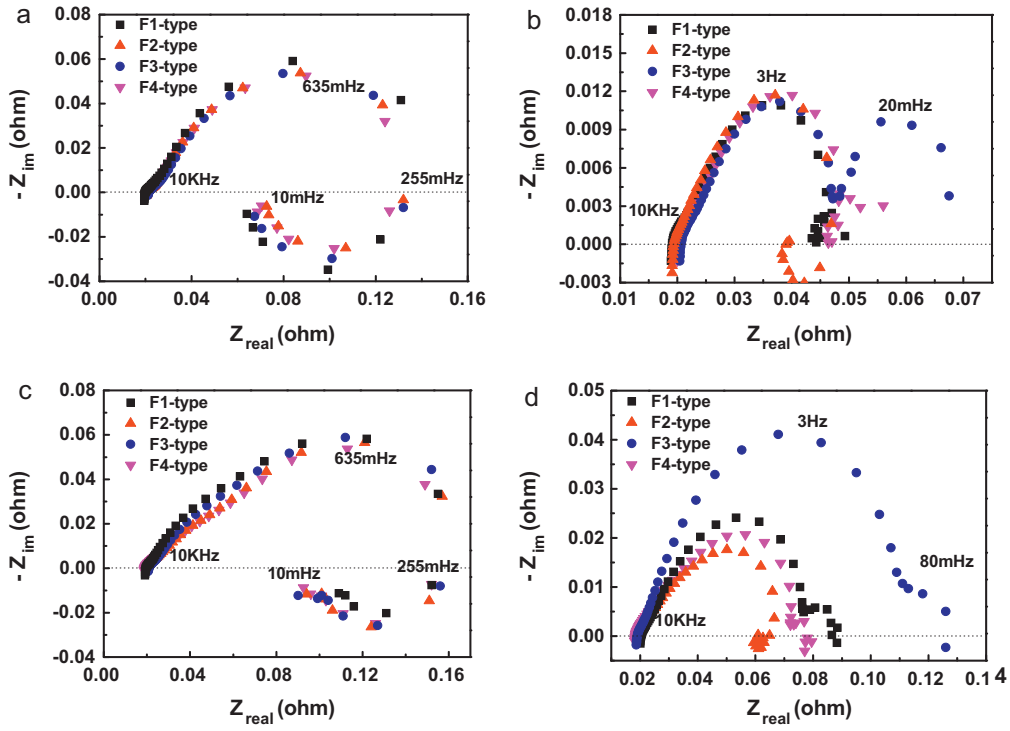

Fig. 7. Experimental Nyquist plots of the impedance spectrum of the cells using different flow channel geometries: anode at a current density of 100 mA cm^{-2} (a) and 400 mA cm^{-2} (b), and complete cells at a current density of 100 mA cm^{-2} (c) and 400 mA cm^{-2} (d).

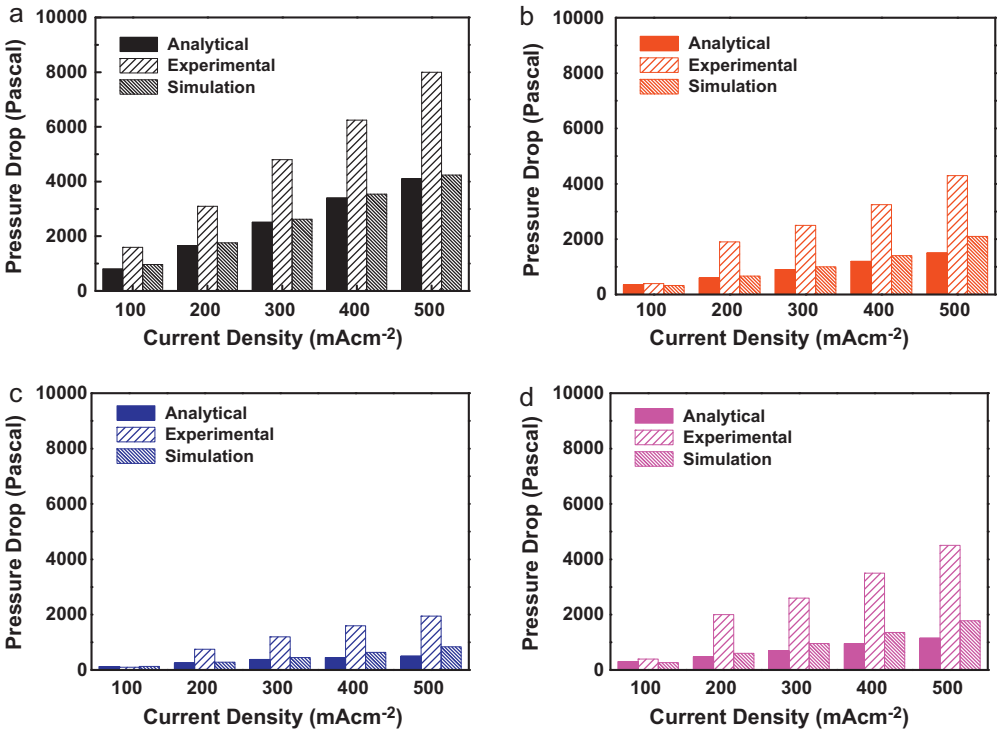

Fig. 8. Experimental and simulated pressure drop in the cathode channel of F1–F4 type geometries at different operating current densities from 100 to 500 mA cm^{-2} with air stoichiometry $\lambda = 3$.

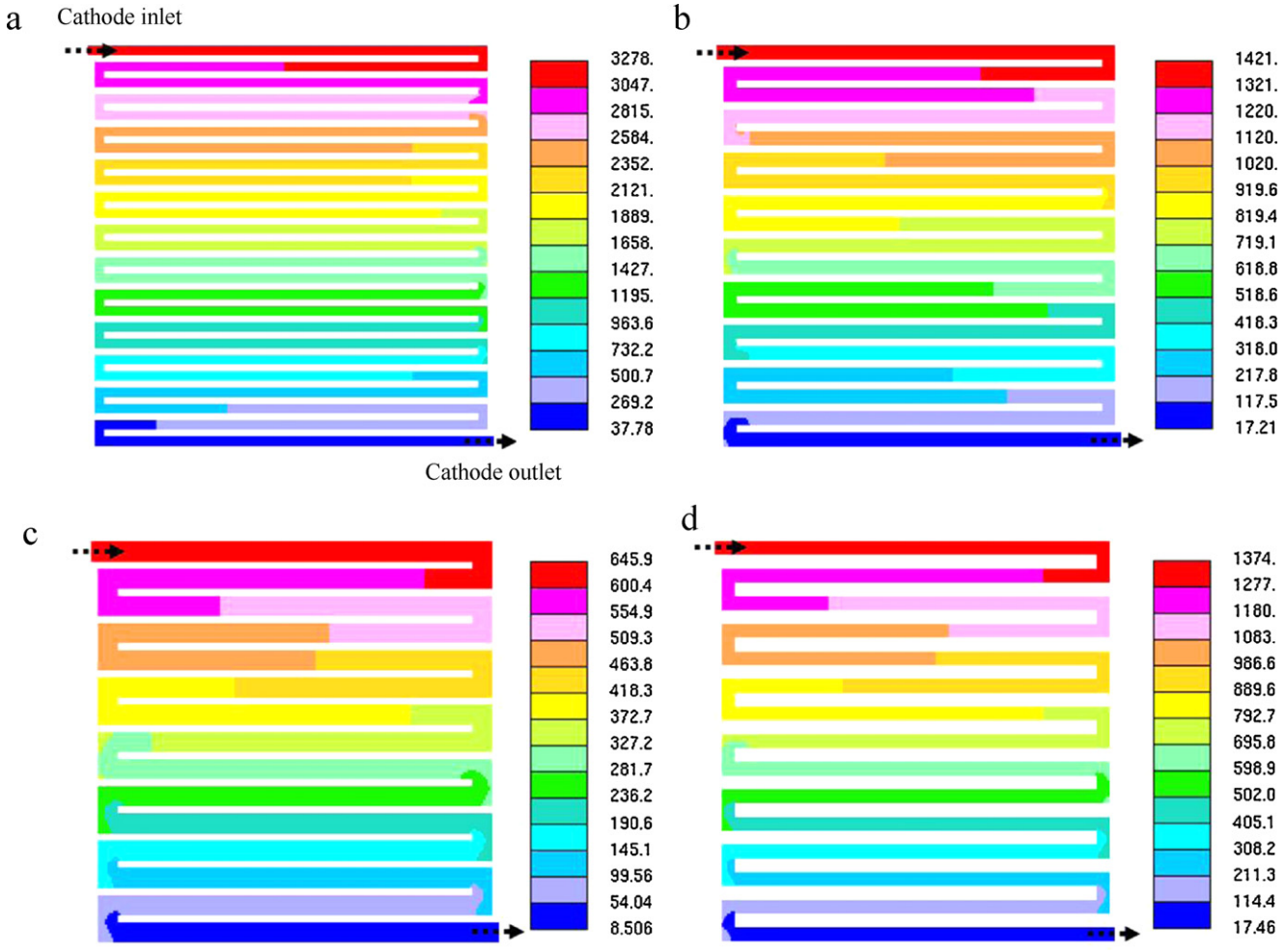

Fig. 9. Simulated pressure contours in the cathode flow channel for (a) Fl-, (b) F2-, (c) F3- and (d) F4-types of geometries.

resistance of the different rib dimensions was only 1.9 mΩ and that the voltage loss corresponding to the ohmic resistance was merely 1.7–6.8 mV ($R_{ohmic} = V_{loss}/iA$). This indicates that the difference in the cell resistance generated by the flow channel geometries less seriously affects the IR loss of the polarization curve. In spite of the different current passage areas of each cell, the cell performance is not greatly affected by the ohmic resistance of the cells [37].

The experimentally measured polarization curves of the anode and cathode shown in Fig. 6 describe the anode and cathode reaction features of the cells with the different flow channel geometries. As presented in Fig. 6, the performance of the cells with these flow channels was primarily determined by the cathode overpotential loss rather than by the anode overpotential loss. The anode polarization curves of all the cells were almost the same in the current density regions below 500 mA cm^{-2}, whereas the cathode polarization curves differed in the current density regions above 300 mA cm^{-2}. The cathode overpotential loss of the cells with F1-, F3-, and F4-type flow channels gradually increase in the current density regions above 300 mA cm^{-2}. This result implies that the performance difference of the cells with these flow channel geometries could primarily be ascribed to mass transport and water removal on the cathode, since convective transport governing mass transport depends on flow channel geometry and flow conditions. However, it is observed that the anode overpotential of F3-type case becomes higher than others above about 500 mA cm^{-2}, which indicates that the F3-type flow channel is not likely to provide sufficient methanol demand for MOR in the high current density region. Although an increase of the channel width would expand the direct contact areas between the methanol and GDL, a broad channel could result in a decrease of the fuel velocity and a pressure drop within the channel, and it finally appears to limit the convection process of supplying fuel under the rib and to remove the produced CO_2 from the cell.

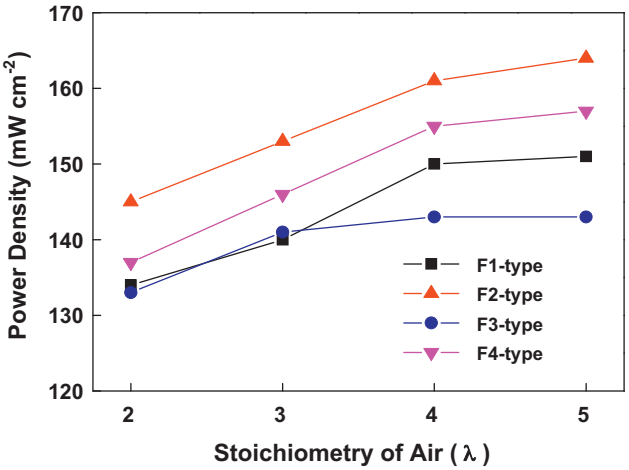

Fig. 10. Experimental power density of the cells according to the stoichiometry of supplied air in the cathode at an operating temperature of 60 °C.

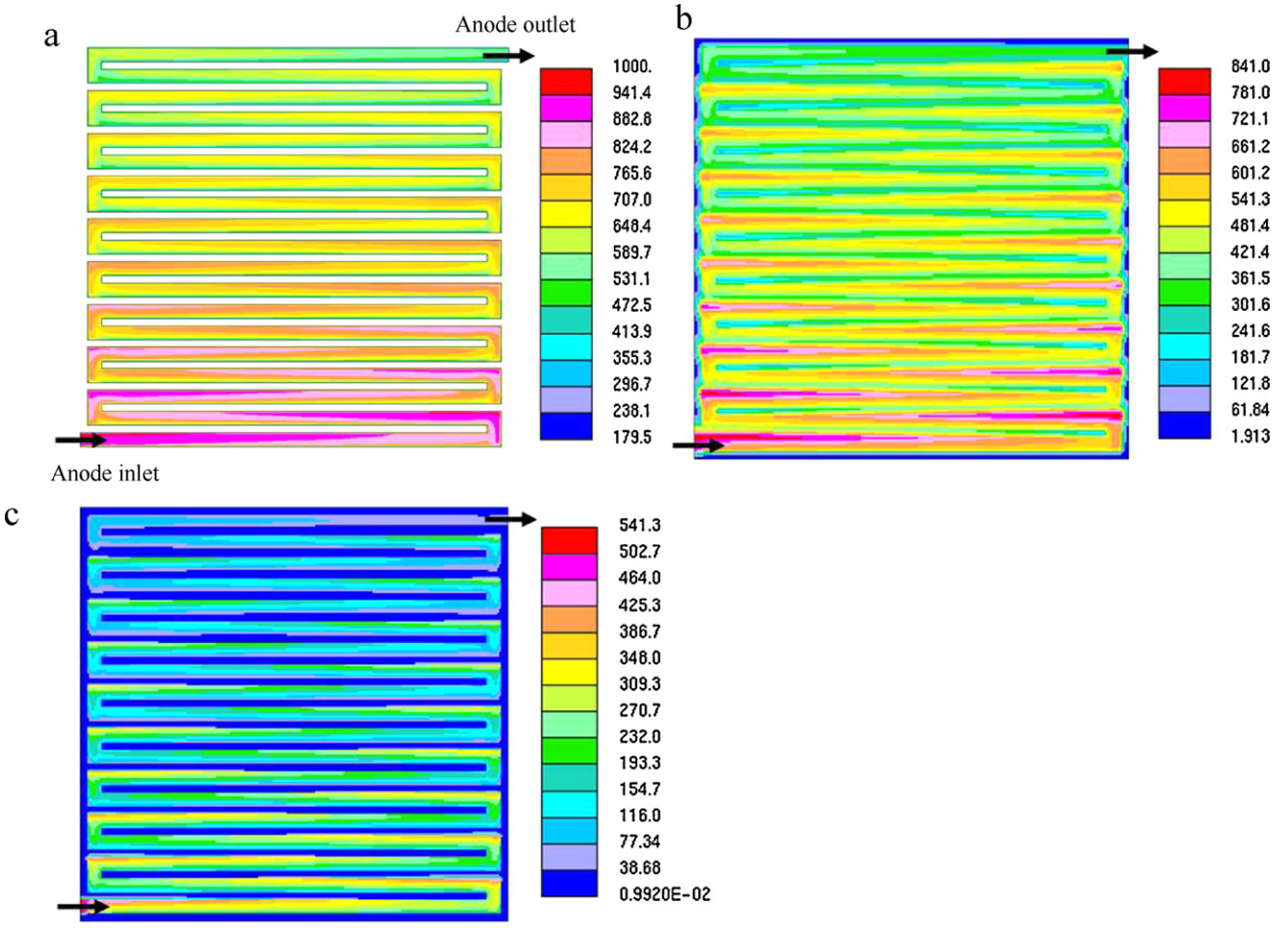

Fig. 11. Simulated methanol concentration contours (mol m^{-3}) in the (a) anode flow channel, (b) anode GDL and (c) anode CL at current density of 400 mA cm^{-2} (F2-type channel).

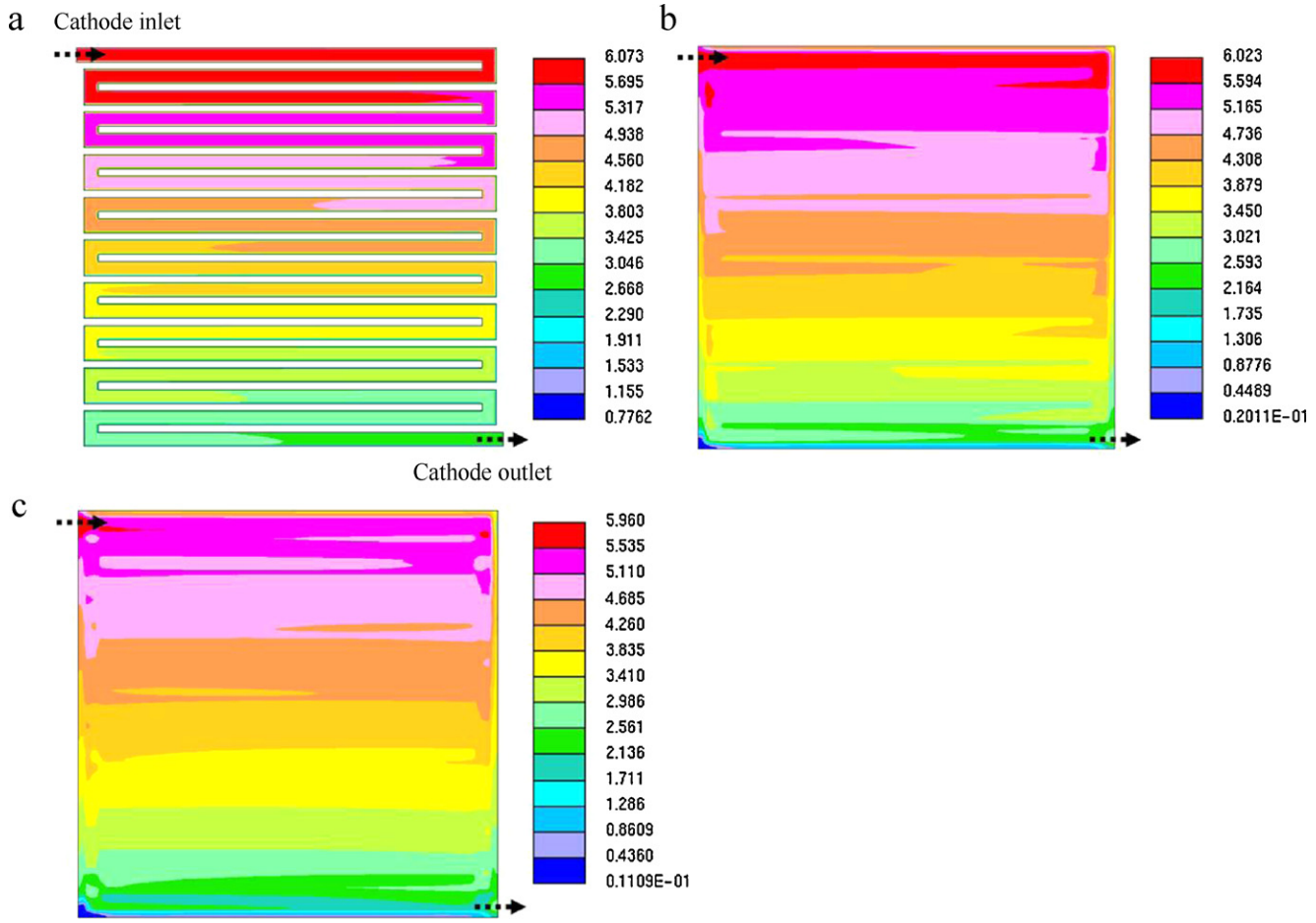

Fig. 12. Simulated oxygen concentration contours (mol m^{-3}) in the (a) cathode flow channel, (b) cathode GDL and (c) cathode CL at current density of 400 mA cm^{-2} (F2-type channel).

Nyquist plots of the impedance spectra for anode and complete cells are experimentally measured to investigate the characteristics of the electrochemical reaction for cells using the different flow channel geometries. Fig. 7(a) and (b) shows the Nyquist plots of the impedance spectra for the anode at a current density of 100 mA cm^{-2} and 400 mA cm^{-2}, respectively, and Fig. 7(c) and (d) for complete cells at a current density of 100 mA cm^{-2} and 400 mA cm^{-2}, respectively. The impedance spectra of the anodes (Fig. 7(a) and (b)) show that the impedance circles mostly coincide at a low current density of 100 mA cm^{-2}, whereas the Nyquist plots at a high current density of 400 mA cm^{-2} are definitely distinguished at low frequencies (below 1 Hz). According to Mueller et al. [38], the low-frequency arc of the anode impedance, which can be observed in the Nyquist plots at frequencies below 1 Hz, is clearly related to the mass transport of methanol in the anode. Thus, the Nyquist plots at a high current density confirm that the F3-type flow channel has a larger mass transport limitation than the other flow channel geometries. This behavior is entirely consistent with the result of the anode polarization curve of Fig. 6. In addition, in the case of the impedance spectra of the complete cells (Fig. 7(c) and (d)), the mass transport limitation from F1-type and F4-type flow channels, as well as from the F3-type flow channel, is observed at a high current density of 400 mA cm^{-2}. These impedance results indicate that the F2-type flow channel exhibits better mass transport capability on both of the anode and cathode than the other types.

The pressure drop of the cathode channel is a very important factor because it affects the two-phase flow associated with water removal and water flooding [39]. A pressure difference between the inlet (p_{in}) and the outlet (p_{out}) drives the fluid flow. Increasing the pressure drop between the inlet (p_{in}) and the outlet (p_{out}) will increase the mean fuel velocity in the channel and improve the convection. However, at extremely high gas velocities, convective mixing may penetrate into the electrode itself, causing the GDL to retreat. Thus, convective transport that dominates mass transport depends on the flow conditions and the flow channel geometry [32]. According to Barbir et al. [40], pressure drop can be used as a diagnostic tool to detect flooding in a fuel cell. The pressure drop in the cathode channel increases with the current density. This is mainly due to either liquid water droplets or water films in the flow channels, which are related to the amount of water that is produced from the oxygen reduction reaction based on Faraday's law [41,42]. In addition to this general fact, it should be noted that the cathode pressure drop could be affected by the flow channel geometry.

Fig. 8 shows the experimentally measured, analytically calculated, and numerically simulated pressure drops along the cathode flow path of F1–F4 type geometries at the operating current densities from 100 to 500 mA cm^{-2} under air stoichiometry of $\lambda = 3$. The analytical pressure drop in the flow channels of the cathode was calculated by the Darcy–Weisbach equation (51), which enables the calculation of the pressure loss due to friction within a given length of the channel. The experimental pressure drop was directly measured from the single cells with the different flow channels. From Darcy–Weisbach equation (51), the analytical pressure drop in the flow channels is linearly proportional to the velocity of the flow and the channel length. This is illustrated well in Table 3 and

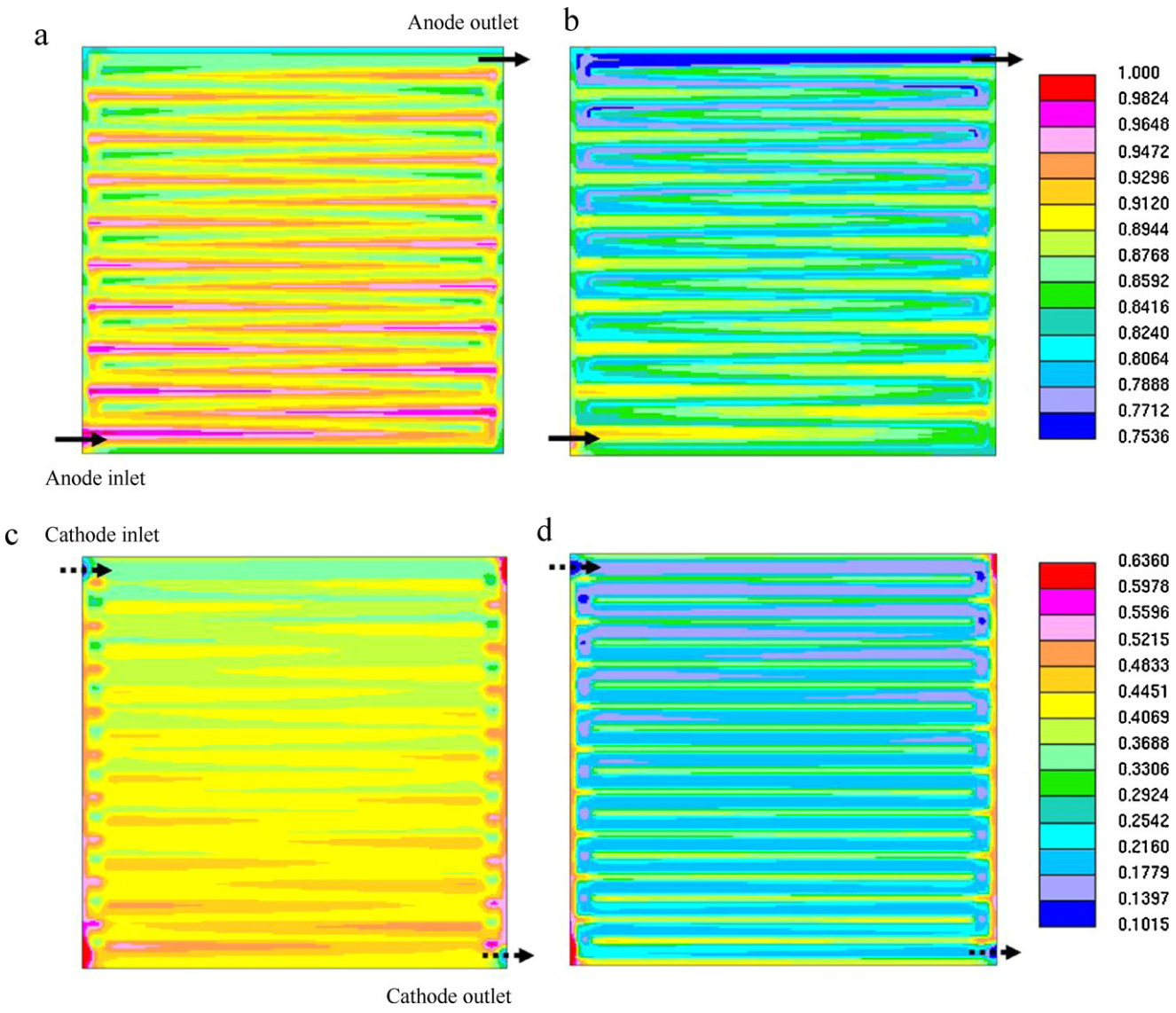

Fig. 13. Simulated liquid saturation contours in the (a) anode GDL, (b) anode CL (c) cathode CL and (d) cathode GDL (F2-type channel).

Fig. 8. Furthermore, the simulated results of Figs. 8 and 9, which show the contour of pressure drop in the cathode channel of F1–F4 type geometries at an operating current density of 400 mA cm^{-2}, exhibit an analogous tendency on the cathode pressure. However, the calculated and simulated pressure drops are smaller than the pressure drop experimentally measured using a nanometer, which indicates that the water flooding in the cathode channel is significant in the experimental cells. As shown in Fig. 8, the pressure drop in the F2-type flow channel is somewhat lower than the pressure drop of the F4-type flow channel, which has the same flow velocity but a shorter channel length than the F2-type flow channel. Generally, during normal operation, liquid water initially accumulates in the GDL under the ribs, as ribs are the coolest location [43]. Yamada et al. [44] found that liquid water accumulated more rapidly under ribs at a higher current density and the liquid water under ribs was more difficult to expel due to its longer transport route. Therefore, considering the relationship between the pressure drop and the two-phase flow in the cathode, this result implies that an F2-type flow channel with a narrow rib eliminates the accumulated liquid water under the ribs more rapidly. In addition, the good water removal capability provides shorter convection routes to supply air quickly at the sites from which the water was removed, which improves the mass transport characteristics in the high current-density region. These characteristics of the F2-type flow channel enable the F2-type channel to have higher cell performance than the other geometric channels. On the other hand, the higher pressure drop of the F1-type flow channel could be caused by the long water column from the narrow channel; the higher pressure drop of the F4-type flow channel could result from the liquid water that accumulated under the ribs and from the longer convection routes due to the broad rib. These phenomena appear to make it much more difficult for the two channels to expel the accumulated liquid water outside the cells. The F3-type flow channel experienced a lower pressure drop in the channel due to a broad channel width and a slow flow velocity, making it more likely to have a dead site under the ribs. Thus, the F2-type flow channel geometry is beneficial for the operation of the cell since because it easily removes excess liquid water from the cell and contributes to mitigating the mass transport problem in a higher current density.

Effects of the stoichiometry of air supplied in the cathode on the experimentally measured power densities of the cells are presented in Fig. 10. Generally, excess air should be supplied to the cathode to sustain the electrochemical reaction and to prevent oxygen starvation; however, this can influence the two-phase flow,

which depends on the pressure drop, fuel distribution, and water flooding. Therefore, the effects of the stoichiometry of air in the cathode can vary with the flow channel geometries. As shown in Fig. 10, the performance of the cells with F1-, F2-, and F4-type flow channels was improved with an increase of the stoichiometry of the supplied air in the cathode. These results show that increasing the stoichiometry of the air in the cathode leads to better fuel distribution and more efficient removal capability of product water. In contrast, the performance of the cell with an F3-type flow channel was not considerably enhanced by increasing the air stoichiometry. It is believed that the lower pressure drop in the flow channel, caused by the broad channel width, leads to difficulty in the supply of the fuel under the rib and in the removal of the produced water from the cell despite the increase in the amount of the air.

4.3. Detailed methanol, air, liquid saturation contours for the F2-type flow channel

Besides the comparison of the predicted results and measured data, multidimensional distributions of methanol, oxygen, and liquid saturation are also obtainable from the simulations and should provide greater insight into the operation of DMFCs. Fig. 11 shows the numerically simulated methanol concentration (mol m^{-3}) on the anode flow channel (Fig. 11(a)), anode GDL (Fig. 11(b)) and anode CL (Fig. 11(c)). The methanol concentration was calculated with F2-type channel geometry (channel width: 1.0 mm, rib width: 0.5 mm) at a current density of 400 mA cm^{-2}. In comparison, the methanol concentration in DMFCs decreases from the anode flow channel (Fig. 11(a)) toward anode CL (Fig. 11(c)) along the through-plane direction. In particular, the steep gradient of methanol concentration between the anode GDL and the anode CL is observed and is due to a limited diffusion rate of methanol from the anode flow channel into the anode CL as well as fast consumption of methanol at the CL. The limited diffusion rate of methanol can be ascribed to presence of the CO_2 gas in the flow channel and GDL. According to Lu et al. [45], the CO_2 gas bubbles are held on the carbon paper by strong surface tension until they grow into larger slugs for detachment. Once the bubbles grow to a sufficient size, they detach and sweep along the GDL surface of the channel. However, when CO_2 gas cannot be removed efficiently from the surface of the backing layer and they remain, the GDL and flow channel blocked by CO_2 gas bubbles and slugs can restrict the through-plane transport of methanol to the anode CL, thereby increasing the concentration polarization [46]. This bubble motion is governed by the momentum of liquid flow as well as the surface adhesion between bubbles and substrate [45]. Thus, the anode flow channel can be an important factor to obtain better mass transport of methanol and CO_2 gas on the DMFC anode. The importance of the flow channel was also confirmed from the in-plane transport of methanol. From Fig. 11(b) and (c), the methanol concentration decreased near the methanol outlet and around the channel ribs. These phenomena are affected by the sub-rib convection of the serpentine flow channel, the flow velocity and the pressure drop. This indicates that the mass transport of methanol and CO_2 gas on the DMFC anode depends on the dynamic mass transfer of the anode flow channel.

Fig. 12 exhibits the numerically simulated air concentration (mol m^{-3}) on the cathode flow channel (Fig. 12(a)), cathode GDL (Fig. 12(b)) and cathode CL (Fig. 12(c)) with F2-type channel geometry. The cell condition is the same as that of Fig. 11. It is seen in Fig. 12 that the oxygen concentration gradient along the through-plane direction is smaller than the methanol concentration (Fig. 11), mainly because of the larger gas-phase diffusivity of oxygen. Fig. 13 displays the liquid saturation contours in both anode and cathode GDLs and CLs for the F2-type channel geometry. It is clearly seen that the liquid phase is dominant in the anode porous region (GDL and CL) whereas the cathode GDL and CL are gas-dominated. The

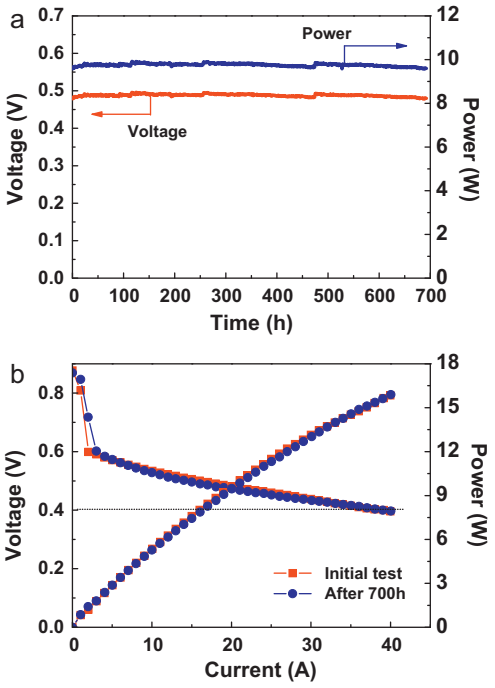

Fig. 14. Experimental long-term stability (Fig. 13(a)) and polarization curves (Fig. 13(b)) of a large cell (150 cm^2) with the F2-type flow channel geometry.

fact further indicates that CO_2 in the anode and water in the cathode are efficiently removed with the F2-type channel geometry.

4.4. Long-term stability test of F2-type flow channel

The experimental results of long-term stability and the polarization curve of a large cell (150 cm^2) with the F2-type flow channel are given in Fig. 14(a) and (b), respectively. The long-term test of the cell was performed with a constant current mode of 20 A (133 mA cm^{-2}) at a methanol flow rate of $\lambda = 2.5$ and an air flow rate of $\lambda = 3.0$ for 700 h. As shown in Fig. 14(a), the large cell with the F2-type flow channel exhibited a constant performance of 9.60 W (0.480 V, 64.0 mW cm^{-2}) for 700 h. At the beginning of the test, the cell provided output power of 9.66 W (0.483 V, 64.4 mW cm^{-2}), and this output was maintained for 700 h. The observed performance loss over the 700 h period was scarcely (9.66 W (0.483 V) → 9.60 W (0.48 V)). This long-term stability of the cell was also confirmed from the polarization curves of the cell before and after the long-term test. As given in Fig. 14(b), the polarization curves of the cell before and after the long-term test for 700 h were almost the same: the performance loss for a nominal voltage of 0.40 V was scarcely (15.65 W (39.13 A, 104.33 mW cm^{-2}) → 15.62 W (39.04 A, 104.13 mW cm^{-2})) after the long-term test of 700 h. These results indicate that the cell with the F2-type flow channel provides good long-term stability as well as high performance (0.4 V, 104.13 mW cm^{-2}).

According to the previous paper [31,47], performance loss of fuel cells in long-term operation mainly originates from cathode degradation caused by electrocatalyst agglomeration or deterioration of mass transport within the GDLs and the CLs. Based on these suggestions, our results suggest that the F2-type flow channel provides very good fuel distribution, mass transport and removal of the products (H_2O and CO_2) in DMFCs during long-term operation.

5. Conclusion

In this study, the effect of flow channel geometry on the performance of DMFCs was numerically and experimentally investigated

using single-path serpentine patterns with different channel widths, rib widths, and channel lengths. In spite of the different current passage areas of each cell, the cell performance was not affected by the resistance of the cells. The anode/cathode polarization curves showed that the performance of the cells with the different flow channel geometries was primarily determined by the cathode overpotential loss rather than by the anode overpotential loss, particularly in the current density regions above 300 mA cm^{-2}. According to impedance spectra, the F2-type flow channel had better mass transport capability in both the anode and cathode sides than the other types. The pressure drops measured in the cathode channel indicated that the F2-type flow channel eliminated liquid water accumulated under the ribs more readily; the good water removal capability also provided short convection routes to supply air quickly at the removed water sites. Finally, such advantages resulted in mass transport improvement of the F2-type flow channel in high current density regions. In addition, the long-term operation test of a large cell (150 cm^2) with the F2-type flow channel showed that performance degradation of the cell hardly occurred for 700 h. This result confirmed that F2-type flow channel provided very good fuel distribution, mass transport and removal of the products (H_2O and CO_2) in a DMFC during long-term operation.

Acknowledgement

This work was supported by the Next Generation Military Battery Research Center program of Defense Acquisition Program Administration and Agency for Defense Development.

References

[1] X. Ren, P. Zelenay, S. Thomas, J. Davey, S. Gottesfeld, J. Power Sources 86 (2000) 111–116.
[2] G. Hoogers, Fuel Cells Technology Handbook, CRC Press, USA, 2003.
[3] M. Baldauf, W. Preidel, J. Power Sources 84 (1999) 161–166.
[4] C.W. Wong, T.S. Zhao, Q. Ye, J.G. Liu, J. Power Sources 155 (2006) 291–296.
[5] R.W. Reeve, G.T. Burstein, K.R. Williams, J. Power Sources 128 (2004) 1–12.
[6] S.Q. Song, Z.X. Liang, W.J. Zhou, G.Q. Sun, Q. Xin, V. Stergiopoulos, P. Tsiakaras, J. Power Sources 145 (2005) 495–501.
[7] J. Zhang, G. Yin, Z. Wang, Y. Shao, J. Power Sources 160 (2006) 1035–1040.
[8] T.V. Reshetenko, H.T. Kim, H. Lee, M. Jang, H.J. Kweon, J. Power Sources 160 (2006) 925–932.
[9] M. Hyun, S.K. Kim, D. Jung, B. Lee, D. Peck, T. Kim, Y. Shul, J. Power Sources 157 (2006) 875–885.
[10] A.P. Manso, F.F. Marzo, M. Garmendia Mujika, J. Barranco, A. Lorenzo, Int. J. Hydrogen Energy 36 (2011) 6795–6808.
[11] S. Shimpalee, J.W. Van Zee, Int. J. Hydrogen Energy 32 (2007) 842–856.
[12] Y.G. Yoon, W.Y. Lee, G.G. Park, T.H. Yang, C.S. Kim, Electrochim. Acta 50 (2004) 709–712.
[13] X.D. Wang, Y.Y. Duan, W.M. Yan, X.F. Peng, J. Power Sources 175 (2008) 397–407.
[14] X.D. Wang, Y.Y. Duan, W.M. Yan, D.J. Lee, A. Sue, P.H. Chi, J. Power Sources 193 (2009) 684–690.
[15] A.P. Manso, F.F. Marzo, M.G. Mujika, J. Barranco, A. Lorenzo, Int. J. Hydrogen Energy 36 (2011) 6795–6808.
[16] H. Yang, T.S. Zhao, Electrochim. Acta 50 (2005) 3243–3252.
[17] C.Y. Wang, P. Cheng, Int. J. Heat Mass Transfer 39 (1996) 3607–3618.
[18] H. Ju, J. Power Sources 191 (2009) 259–268.
[19] H. Ju, J. Power Sources 185 (2008) 55–62.
[20] K. Kang, H. Ju, J. Power Sources 194 (2009) 763–773.
[21] J. Nam, P. Chippar, W. Kim, H. Ju, Applied Energy 87 (2010) 3699–3709.
[22] P. Chippar, O. Kyeongmin, K. Knag, H. Ju, Int. J. Hydrogen Energy, doi:10.1016/j.ijhydene.2011.04.154.
[23] R.B. Bird, W.E. Stewart, E.N. Lightfoot, Transport Phenomena, John Wiley & Sons, 1960.
[24] E. Springer, T.A. Zawodzinski, S. Gottesfeld, J. Electrochem. Soc. 138 (1991) 2334–2342.
[25] J.P. Meyers, J. Newman, J. Electrochem. Soc. 149 (2002) A710–A717.
[26] J.P. Meyers, J. Newman, J. Electrochem. Soc. 149 (2002) A718–A728.
[27] J.P. Meyers, J. Newman, J. Electrochem. Soc. 149 (2002) A729–A735.
[28] Z.H. Wang, C.Y. Wang, J. Electrochem. Soc. 150 (2003) A508–A519.
[29] A. Parthasarathy, S. Srinivasan, A.J. Appleby, J. Electrochem. Soc. 139 (1992) 2530–2537.
[30] CD-Adapco Group, STAR-CD Version 4.00 Methodology, USA, 2006.
[31] Y.C. Park, S. Kang, S.K. Kim, S. Lim, D.H. Jung, D.Y. Lee, Y.G. Shul, D.H. Peck, Int. J. Hydrogen Energy 36 (2011) 15313–15322.
[32] F. Barbir, PEM Fuel Cells: Theory and Practice, Elsevier Academic Press, London, UK, 2005, pp. 170–177.
[33] C.L. Yaws, Handbook of transport property data: viscosity, thermal conductivity, and diffusion coefficients of liquids and gases, Gulf Pub Co., Houston, TX, 1995.
[34] E.L. Cussler, Diffusion: Mass transfer in fluid systems, Cambridge University Press, New York, 1984.
[35] X. Ren, T.E. Springer, T.A. Zawodzinski, S. Gottesfeld, J. Electrochem. Soc. 147 (2000) 466–474.
[36] W.W. Yang, T.S. Zhao, C. Xu, Electrochim. Acta 53 (2007) 853–862.
[37] G.B. Jung, A. Su, C.H. Tu, Y.T. Lin, F.B. Weng, S.H. Chan, J. Power Sources 171 (2007) 212–217.
[38] J.T. Mueller, P.M. Urban, J. Power Sources 75 (1998) 139–143.
[39] T.E. Springer, M.S. Wilson, S. Gottesfeld, J. Electrochem. Soc. 140 (1993) 3513–3526.
[40] F. Barbir, H. Gorgun, X. Wang, J. Power Sources 141 (2005) 96–101.
[41] X. Liu, H. Guo, C. Ma, J. Power Sources 156 (2006) 267–280.
[42] X. Liu, H. Guo, F. Ye, C. Ma, Electrochim. Acta 52 (2007) 3607–3614.
[43] P. Liua, G.P. Yina, K.D. Cai, Electrochim. Acta 54 (2009) 6178–6183.
[44] R.H. Yamada, T. Hatanaka, H. Murata, Y. Morimoto, J. Electrochem. Soc. 153 (2006) A1748–A1754.
[45] G.Q. Lu, C.Y. Wang, J. Power Sources 134 (2004) 33–40.
[46] T.S. Zhao, C. Xu, R. Chen, W.W. Yang, Prog. Energy Combust. Sci. 35 (2009) 275–292.
[47] H.C. Cha, C.Y. Chen, J.Y. Shiu, J. Power Sources 192 (2009) 451–456.